

# Thermal Instability and Self-Sustained Modulation in Superconducting NbN Stripline Resonators

Eran Segev,\* Baleegh Abdo, Oleg Shtempluck, and Eyal Buks

*Microelectronics Research Center, Department of Electrical Engineering, Technion, Haifa 32000, Israel*

(Dated: June 28, 2018)

We study theoretically and experimentally the response of a microwave superconducting stripline resonator, integrated with a microbridge, to a monochromatic injected signal. We find that there is a certain range of driving parameters, in which a novel nonlinear phenomenon emerges, and self-sustained modulation of the reflected power off the resonator is generated by the resonator. A theoretical model which attributes the self modulation to a thermal instability yields a good agreement with the experimental results.

PACS numbers: 74.40.+k, 85.25.Am

## I. INTRODUCTION

Nonlinear effects in superconductors have significant implications for both basic science and technology. Strong nonlinearity may be exploited to study some important quantum phenomena in the microwave region, such as quantum squeezing<sup>1,2,3</sup> and experimental observation of the so called dynamical Casimir effect<sup>4</sup>. These effects may also allow some intriguing technological applications such as bifurcation amplifiers for quantum-limited measurements<sup>5,6</sup>, resonant readout of qubits<sup>7</sup>, mixers<sup>8</sup>, single photon detectors<sup>9</sup>, and more.

In this paper we study theoretically and experimentally the response of a superconducting (SC) microwave stripline resonator, designed for enhanced nonlinearity, to a monochromatic injected signal. We find that there is a certain range of driving parameters, in which a novel nonlinear phenomenon emerges, and self-sustained modulation (SM), of the reflected signal from the resonator, is generated. That is, the resonator undergoes limited cycle oscillations, ranging between several to tens of megahertz. Similar phenomenon was briefly reported in the 60's<sup>10,11,12,13</sup> in dielectric resonators which were partially coated by a SC film, but it was not thoroughly investigated and its significance was somewhat overlooked. This phenomenon is of a significant importance as it introduces an extreme nonlinearity, which is by far stronger than any other nonlinearity observed before in SC resonators<sup>14</sup>. It results in a very strong intermodulation gain, strong noise squeezing and period doubling of various orders<sup>14</sup>, strong coupling between different resonance modes<sup>15</sup>, and more.

The central results of this study have been recently reported in a short paper<sup>15</sup>. In this paper we extend the previous report and derive a theoretical model, according to which the SM originates by a thermal instability in the resonator. The numerical integration of the model's equations of motion exhibits SM, which have similar characteristics as the experimental results. In addition, we derive analytic expressions for the expected SM frequency and the spectral power density. These expressions also yield a good agreement with the experi-

mental results.

This paper is organized as follows. First we briefly describe the design of our devices and the experimental setup. Then we present the SM phenomenon, as measured in our devices. Afterwards, we derive the theoretical model, discuss and justify its underlying assumptions and present the numerical integration results. Finally, we quantitatively compare the predictions of the model to typical experimental results.

## II. EXPERIMENTAL SETUP AND CIRCUIT DESIGN

The majority of the experiments are performed using the experimental setup described in Fig. 1(a). The resonator is stimulated with a monochromatic pump tone at an angular frequency  $\omega_p$ . The power reflected off the resonator is amplified at room temperature and measured by using both a spectrum analyzer (SA) in the frequency domain, and an oscilloscope, tracking the reflected power envelope in the time domain. In other experiments, the  $|S_{11}|$  reflection coefficient is measured using a network analyzer (NA), connected directly to the resonator RF port. All measurements are carried out while the device is fully immersed in liquid Helium.

A simplified circuit layout of the device is illustrated in Fig. 1(b). The resonator is designed as a stripline ring<sup>16,17</sup>, having a characteristic impedance of  $50\Omega$ . It is composed of Niobium Nitride (NbN) deposited on a Sapphire wafer. The first few resonance frequencies fall within the range of 2–8 GHz. A feedline, weakly coupled to the resonator, is employed for delivering the input and output signals. A microbridge, which is employed as a weak-link that allows the manipulation of the resonator's resonance frequencies<sup>18</sup>, is monolithically integrated into the structure of the ring. Its angular location, relative to the feedline coupling location, maximizes the RF current amplitude flowing through it in one of the resonance modes, and thus maximizes its coupling to that mode. Further design considerations, fabrication details as well as normal modes calculation can be found elsewhere<sup>16</sup>.

The results presented herein are obtained using two

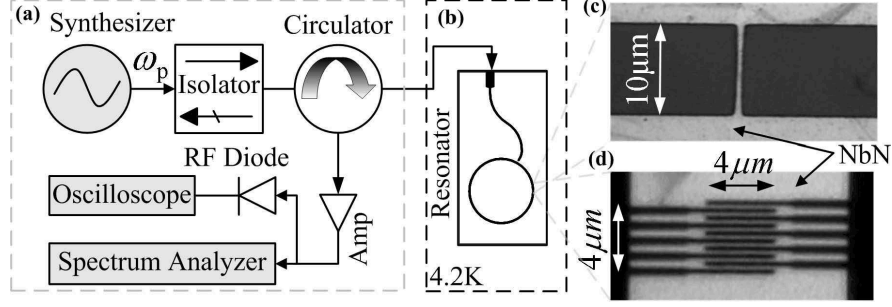


FIG. 1: (a) SM measurement setup. (b) Schematic layout of the device. Subplot (c) and (d) exhibit optical microscope images of the straight and meander shaped microbridges respectively.

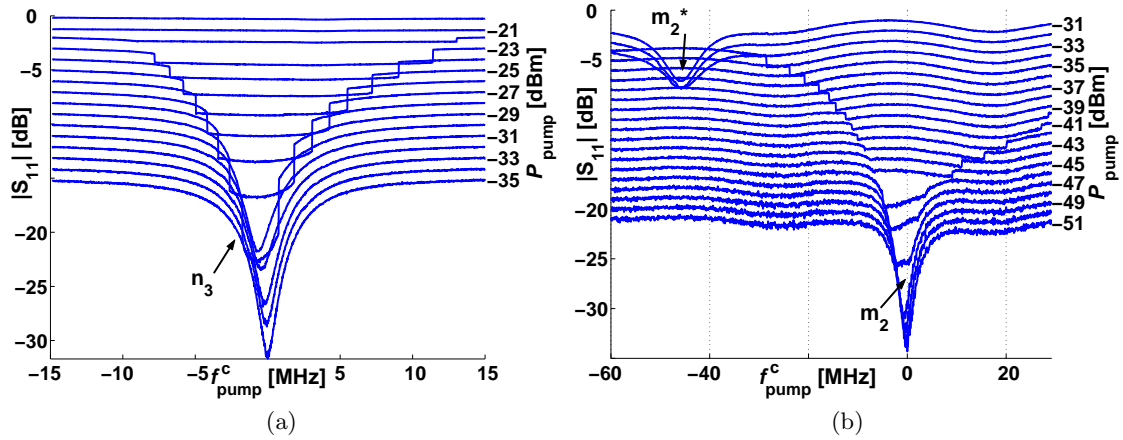


FIG. 2: (Color Online)  $|S_{11}|$  reflection measurements taken with (a) E15 and (b) E16 devices. Note that the  $|S_{11}|$  reflection coefficient is only defined for the case of a steady state reflection from a device. Therefore the  $|S_{11}|$  measurements taken at the SM region should be interpreted as an average over time of the  $|S_{11}|$  coefficient.

distinct devices, labeled as E15 and E16, which differ by the geometry of the microbridges and by their thicknesses. E15 has a  $1 \times 10 \mu\text{m}^2$  microbridge geometry (Fig. 1(c)) and a thickness of 200 nm, whereas E16 has a  $4 \times 4 \mu\text{m}^2$  meander shaped microbridge geometry (Fig. 1(d)) and a thickness of 8 nm. The meander consists of nine strips, where each strip has a characteristic area of  $0.15 \times 4 \mu\text{m}^2$  and the strips are separated one from another by approximately  $0.25 \mu\text{m}^{19}$ .

The difference in the frequency response between E15 and E16 can be observed in a simple  $|S_{11}|$  reflection measurement, obtained using a NA. Fig. 2 shows various  $|S_{11}|$  curves as a function of the pump frequency centralized on the third resonance frequency  $f_3 = 5.666$  GHz of E15 (panel (a)) and the second resonance frequency  $f_2 = 3.87$  GHz of E16 (panel (b)), labeled by  $n_3$  and  $m_2$  respectively. Each curve represents a measurement with a different pump input power. For clarity, the curves are vertically shifted upwards, for increasing power values. The anomaly of the response is described as follows.

Above some power threshold the  $|S_{11}|$  line-shapes cease having a normal Lorentzian shape, their values substantially increase, and the resonance curves substantially broaden and have steep edges. This behavior continues and intensifies as the pump power further increases, until eventually no resonance is detected. Furthermore, as seen in panel (b), at relatively high power levels, the resonance curve of E16 is reconstructed at a new resonance frequency, red shifted by approximately 45 MHz relative to  $f_2$ . The Lorentzian line-shape of the new resonance frequency, labeled by  $m_2^*$ , represents a linear behavior in that power range. These experimental results suggest that external stimulation can cause a significant resonance shift in E16, while E15 can only experience an increase in its damping rate.

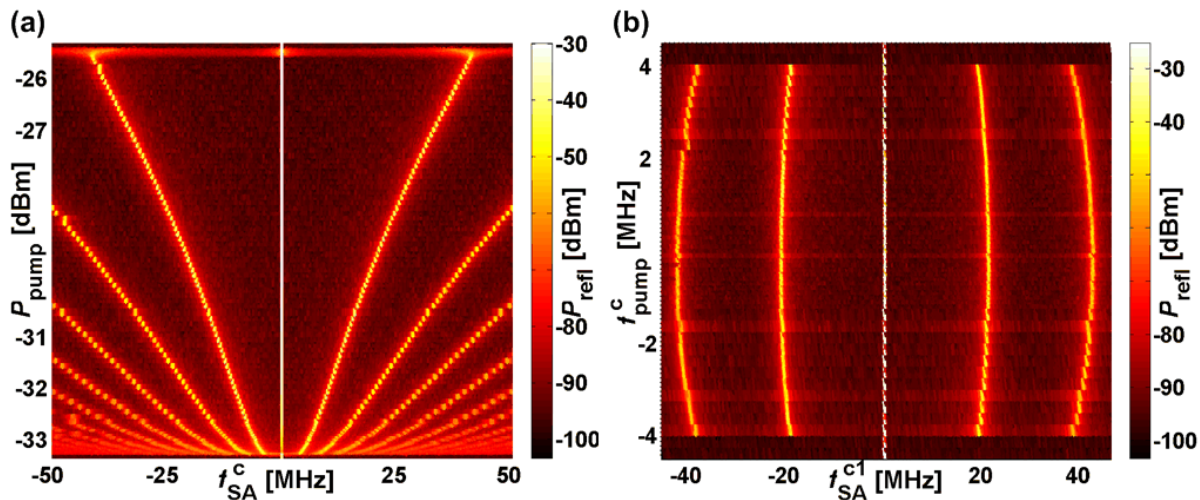


FIG. 3: (Color online) Typical experimental results of the SM phenomenon in the frequency domain. Panel (a) plots a colormap of the reflected power  $P_{\text{refl}}$  as a function of the pump power  $P_{\text{pump}}$  and the measured frequency  $f_{\text{SA}}$  centralized on the third resonance frequency  $f_3$  ( $f_{\text{SA}}^c = f_{\text{SA}} - f_3$ ) of E15, while the resonator is stimulated with a monochromatic pump at  $f_3$ . Panel (b) plots a colormap of the reflected power as a function of the centralized measured frequency around the pump frequency  $f_{\text{SA}}^{c1} = f_{\text{SA}} - \omega_p/2\pi$  and the centralized pump frequency around the resonance frequency  $f_{\text{pump}}^c = \omega_p/2\pi - f_3$ . The resonator is stimulated by a monochromatic pump having a power of  $P_{\text{pump}} = -29.35$  dBm which drives the resonator into the regular SM zone.

### III. SM EXPERIMENTAL OBSERVATION

We now turn to investigate the region where SM emerges. Fig. 3 shows typical experimental results of the SM phenomenon in the frequency domain, as measured with E15. The dependence of the SM on the pump power is shown in panel (a) and described as follows. At low input powers, approximately below  $-33.25$  dBm, and at high input powers, approximately above  $-25.0$  dBm, the response of the resonator is linear, namely, the reflected power from the resonator contains a single spectral component at the frequency of the stimulating pump tone  $\omega_p$ . In between the two linear regions, there is a rather large power range in which regular SM of the reflected power from the resonator occurs. It is realized by rather strong and sharp sidebands, which extend over several hundreds megahertz at both sides of the resonance frequency. The SM frequency, which is defined as the frequency difference between the pump and the primary sideband, increases as the pump power increases.

The regular SM starts and ends at two power thresholds, referred to as the first and the second power thresholds. The first power threshold occurs at a very narrow power range of approximately  $10$  nW, during which the resonator's response desists being linear. It experiences a strong amplification of the noise floor, known also as noise rise, over a rather large frequency band, especially around the resonance frequency itself. The second power threshold occurs on a slightly larger power range than the first one and has similar, but less extreme characteristics.

As shown in panel (b), the dependence of the SM on the pump frequency is rather symmetric around the

resonance frequency. It occurs only within a well defined frequency range around the resonance frequency. A small change in the pump frequency can abruptly ignite or quench the SM. Once started though, the modulation frequency has a relatively weak dependence on the pump frequency. E16 exhibits similar behavior, with slightly different properties, as discussed below in section IV A 3 b.

### IV. THERMAL INSTABILITY

In this section we propose a theoretical model according to which the SM originates by a thermal instability in the SC stripline resonator. Current-carrying superconductors are known to have two metastable phases sustained by Joule self-heating<sup>20</sup>. One phase is the SC phase and the other is an electrothermal local phase, known as hotspot, which is basically an island of normal-conducting (NC) domain, with a temperature above the critical one, surrounded by a SC domain. This phenomenon can be explained by the heat balance equation holding at more than one temperature. Due to an external<sup>21</sup> or internal<sup>22</sup> perturbation, the hotspot can recover to the SC phase or vice versa and thus oscillates between these phases. Such self-sustained oscillations were often observed in experiments, for the case of a SC microbridge driven by an external dc voltage or current (see review<sup>20</sup> and references therein).

In the present case, as the microbridge is integrated into a stripline resonator, the system is driven into instability via externally injected microwave pump tone.

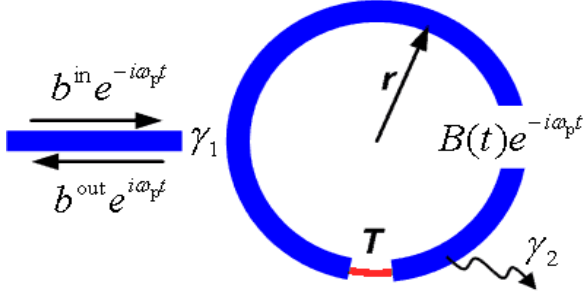


FIG. 4: (Color online) Schematic model of the driven resonator.

Nonlinearity, according to our simple theoretical model, results from the coupling between the equation of motion of the mode amplitude in the resonator (Eq. (1)), and the thermal balance equation (Eq. (3)) in the microbridge. The mechanism presented in this model is somewhat similar to one of the mechanisms which cause self oscillations in an optical parametric oscillator<sup>23</sup>.

### A. Equations of Motion

This section presents the equations of motion of the mode amplitude in the resonator and the thermal balance in the microbridge. Note that Eqs. (1)-(3), (5)-(10) also appear in Ref.<sup>24</sup>, and are re-presented here to ensure that the paper is self-contained.

#### 1. Mode Amplitude

Consider a resonator that is driven by a weakly coupled feedline carrying an incident coherent tone  $a^{\text{in}} = b^{\text{in}} e^{-i\omega_p t}$ , where  $b^{\text{in}}$  is a constant complex amplitude ( $|b^{\text{in}}|^2 \propto P_{\text{pump}}$ , where  $P_{\text{pump}}$  is the driving power) and  $\omega_p$  is the driving angular frequency (See Fig. 4). The mode amplitude inside the resonator can be written as  $A = B(t) e^{-i\omega_p t}$ , where  $B(t)$  is a complex amplitude which is assumed to vary slowly on a time scale of  $1/\omega_p$ . In this approximation, the equation of motion of  $B$  reads<sup>2</sup>

$$\frac{dB}{dt} = [i(\omega_p - \omega_0(T)) - \gamma(T)] B - i\sqrt{2\gamma_1} b^{\text{in}} + c^{\text{in}}, \quad (1)$$

where  $\omega_0(T)$  is the temperature dependant angular resonance frequency,  $T$  is the temperature of the hotspot,  $\gamma(T) = \gamma_1 + \gamma_2(T)$ , where  $\gamma_1$  is the coupling constant between the resonator and the feedline, and  $\gamma_2(T)$  is the temperature dependant damping rate of the mode.

The term  $c^{\text{in}}$  represents an input Gaussian noise with a zero-mean and a random phase, thus  $\langle c^{\text{in}} \rangle = 0$ ,  $\langle c^{\text{in}}(t) c^{\text{in}}(t') \rangle = \langle c^{\text{in}*}(t) c^{\text{in}*}(t') \rangle = 0$ , and its autocorrelation function is given by  $\langle c^{\text{in}}(t) c^{\text{in}*}(t') \rangle =$

$G\omega_0\delta(t - t')$ . Consider the case of relatively high temperature,  $k_B T_{\text{eff}} \gg \hbar\omega_0$ , where  $k_B$  is Boltzmann's constant, and  $T_{\text{eff}}$  is a weighted average between  $T$  and  $T_0$ , where  $T_0$  is the temperature of the coolant and the weight factors are discussed in Ref.<sup>4</sup>. Then at steady state, the variance of the noise is given by  $G = 2\gamma k_B T_{\text{eff}} / \hbar\omega_0^2$ .

The steady state solution of Eq. (1), which is denoted as  $B_\infty$ , is given by

$$B_\infty = \frac{i\sqrt{2\gamma_1} b^{\text{in}}}{i(\omega_p - \omega_0) - \gamma}. \quad (2)$$

#### 2. Thermal Balance

Consider the case where the nonlinearity originates by a local hotspot in the resonator's microbridge. If the hotspot is assumed to be sufficiently small, its temperature  $T$  can be considered as homogeneous. The temperature of other parts of the resonator is assumed be equal to that of the coolant  $T_0$ . The power  $Q$  heating up the hotspot is given by  $Q = \kappa Q_t$ , where  $Q_t = \hbar\omega_0 2\gamma_2 |B|^2$  is the total power dissipated in the resonator, and  $0 \leq \kappa \leq 1$  represents the portion of the dissipated power that is being absorbed by the microbridge. The heat balance equation reads

$$C \frac{dT}{dt} = Q(B) - W, \quad (3)$$

where  $C$  is the thermal heat capacity,  $W = H(T - T_0)$  is the heat transfer power to the coolant, and  $H$  is the heat transfer coefficient.

The steady state solution of Eq. (3), which is denoted as  $T_\infty$ , for  $B = B_\infty$ , is given by

$$T_\infty = T_0 + \frac{\kappa \hbar \omega_0 2\gamma_2 |B_\infty|^2}{H} \quad (4)$$

#### 3. Stability zones

*a. Coupling mechanism* The coupling mechanism between Eq. (1) and Eq. (3) is based on the dependence of both the resonance frequency and the damping rate of the driven mode on the resistance of the microbridge<sup>18</sup>, which in turn depends on the temperature  $T$ <sup>16</sup>.

Here we assume the simplest case, where the resonance frequency  $\omega_0$ , and the damping rate  $\gamma_2$  have a step function dependence on the temperature of the hotspot (the step occurs at the critical temperature  $T_c$ ). It is based on the fact that recent experiments with photodetectors, based on a thin layer of NbN, have demonstrated an intrinsic switching time on the order of 30 ps (see Ref.<sup>9</sup> and references therein). In addition, when illuminating our devices with a power modulated infrared light in a similar way to the experiment described in Ref.<sup>16</sup>, we measure

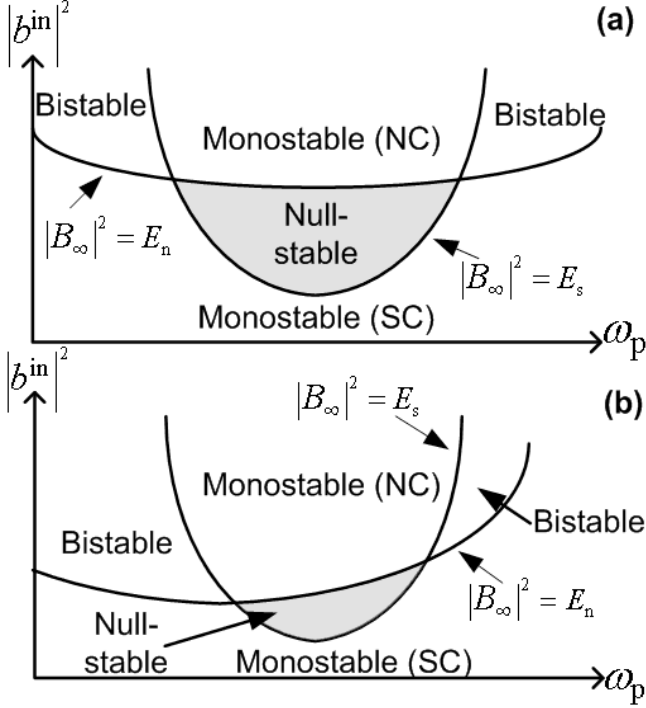


FIG. 5: Stability zones of the system, corresponding to (a) E15 and (b) E16 related assumptions. The solid lines are obtained from Eq. (2) using  $|B_\infty|^2 = E_s$  and  $|B_\infty|^2 = E_n$ .

a clear response up to modulation frequencies of several gigahertz with E16<sup>4</sup> and several hundred megahertz with E15. Thus the transition through the instability point is very fast on the time scale of the SM frequency. We further assume that all other parameters in the model are temperature independent.

Under this assumption, the heat generation on the temperature  $T$  have step-like dependence<sup>20</sup>. The system thus may have in general up to two locally stable steady states, corresponding to the SC and NC phases. A SC steady state exists when  $T_\infty < T_c$ , or alternatively when  $|B_\infty|^2 < E_s$ , where  $E_s = H(T_c - T_0)/2\kappa\gamma_{2s}\hbar\omega_0$ . Similarly, a NC steady state exists when  $T_\infty > T_c$ , or alternatively when  $|B_\infty|^2 > E_n$ , where  $E_n = H(T_c - T_0)/2\kappa\gamma_{2n}\hbar\omega_0$ , where the subscript (s) and (n) denote the value of the corresponding parameter when the system is in the SC and the NC phases respectively.

**b. Stability** The stability of each of these phases depends on both the power and frequency parameters of the injected pump tone, as described by the stability diagrams in Fig. 5. Panel (a) shows a case similar to E15, where the SC and the NC phases differ by the damping rate value, which has a larger value in the latter phase. Panel (b), on the other hand, shows a case similar to E16, where the resonance frequency in the SC phase is higher than the one in the NC phase, whereas the damping rates are the same in both phases.

Four different stability zones can be identified in the

diagram. In the monostable zone either the SC phase or the NC phase is locally stable, whereas in the bistable zones both phases are locally stable<sup>24,25</sup>. In the null-stable zone, on the other hand, none of the phases are locally stable, and the resonator is expected to oscillate between these two phases. As the two phases significantly differ in their reflection coefficients, the oscillations are translated into a modulation of the reflected pump tone. Note that, the stability diagram indicates the existence of both power and frequency hysteresis in the system's response<sup>24,25</sup>. Furthermore, panel (b) in fig. 5 shows that the dependence of the SM on the pump frequency is asymmetric in the case where a resonance frequency shift occurs.

This asymmetry is indeed observed experimentally when measuring the SM frequency as a function of the pump frequency and power as shown in Fig. 6 panels (a) and (b), presenting data obtained with E15 and E16 respectively. In both cases SM occurs in the nullstability zone (compare with Fig. 5). One clearly notices that the SM, as measured with E16, is strongly asymmetric in frequency in contrast to the case of E15. The maximum measured SM frequency is approximately 41.1 MHz and 57.6 MHz with E15 and E16, respectively.

## B. Adiabatic Approximation

In the following section we derive two analytic expressions, one for the SM period (Eq. (22)) and another for the SM spectral density (Eq. (26)). Both expressions are valid for input powers that are slightly larger than the first power threshold. The derivation assumes that the system is in the adiabatic regime, namely that the rate in which the temperature of the hotspot changes is much faster than the SM frequency. In addition it assumes for simplicity that the pump frequency equals the resonance frequency.

### 1. Dimensionless variables

In terms of the dimensionless time  $\tau = \omega_0 t$  Eq. (1) reads

$$\frac{db}{d\tau} + \lambda b = \frac{c^{\text{in}}}{\omega_0}, \quad (5)$$

where  $b = B - B_\infty$ , and  $\lambda = [\gamma - i(\omega_p - \omega_0)]/\omega_0$ .

Defining the dimensionless temperature  $\Theta = (T - T_0)/(T_c - T_0)$ , and using the dimensionless time  $\tau$  Eq. (3) reads

$$\frac{d\Theta}{d\tau} + g(\Theta - \Theta_\infty) = 0, \quad (6)$$

where

$$\Theta_\infty = \frac{2\hbar\kappa\gamma_2|B|^2}{gC(T_c - T_0)} = \frac{2\kappa\gamma_2\rho|B|^2}{\omega_0 g} \quad (7)$$



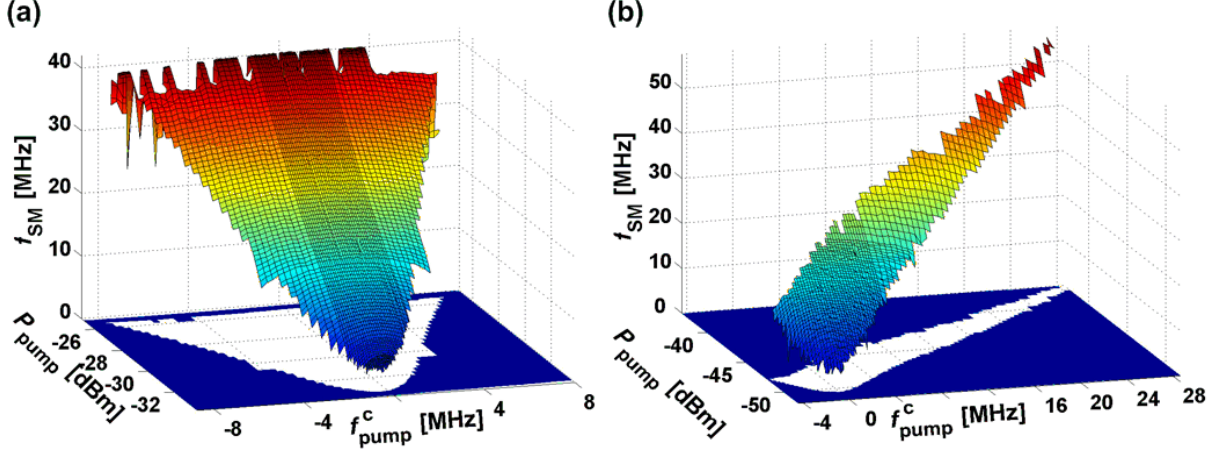


FIG. 6: (Color online) Measured SM frequency  $f_{\text{sm}}$  as a function of the pump power  $P_{\text{pump}}$  and the pump frequency  $f_{\text{pump}}^c$ , centralized on (a) the third and (b) the second resonance frequencies of E15 and E16, respectively.

is the steady state value of the dimensionless temperature for a fixed mode amplitude, and

$$g = \frac{H}{C\omega_0}, \quad (8)$$

$$\rho = \frac{\hbar\omega_0}{C(T_c - T_0)}. \quad (9)$$

The steady states solution of Eq. (6), where  $B = B_\infty$ , is denoted as

$$\Theta_{\infty 0} = \frac{2\hbar\kappa\gamma_2 |B_\infty|^2}{gC(T_c - T_0)} = \frac{2\kappa\gamma_2\rho |B_\infty|^2}{\omega_0 g}. \quad (10)$$

### 2. Adiabatic Solution

Assuming the case where  $\Theta \neq 1$  in the time interval  $(0, \tau)$ , and disregarding noise, the solution of Eq. (5) is given by

$$B(\tau) = B_\infty \left[ 1 + \frac{B(0) - B_\infty}{B_\infty} \exp(-\lambda\tau) \right], \quad (11)$$

thus, using the notation  $\beta = (B(0) - B_\infty)/B_\infty$  and Eq. (10), one has

$$\begin{aligned} \Theta_\infty(\tau') &= \Theta_{\infty 0} [1 + \beta \exp(-\lambda\tau') + \\ &\quad + \beta^* \exp(-\lambda^*\tau') + \\ &\quad + |\beta|^2 \exp[-(\lambda + \lambda^*)\tau']]. \end{aligned} \quad (12)$$

In the adiabatic limit, where  $\gamma/g\omega_0 \ll 1$ , one expects that the temperature closely follows the evolution of the mode amplitude, namely  $\Theta(\tau) \simeq \Theta_\infty(\tau)$ , thus it is convenient to rewrite Eq. (6) as

$$\frac{d\xi}{d\tau} + g\xi = -\frac{d\Theta_\infty}{d\tau}, \quad (13)$$

where  $\xi(\tau) = \Theta(\tau) - \Theta_\infty(\tau)$ . Using Eq. (12) the solution of Eq. (13) for the case  $g\tau \gg 1$  can be written as

$$\Theta(\tau) = \Theta_\infty(\tau) - \frac{1}{g} \frac{d\Theta_\infty(\tau)}{d\tau}. \quad (14)$$

Thus the lagging of the temperature  $\Theta(\tau)$  behind the asymptotic value  $\Theta_\infty$  depends on the rate of change of  $|B|^2$  (see Eq. (7)).

Moreover, when the pump frequency equals the resonance frequency, namely  $\omega_p = \omega_0$ ,  $B$  is purely imaginary and its time evolution is given by

$$\frac{B(t) - B_\infty}{B(0) - B_\infty} = \exp\left(-\frac{\gamma\tau}{\omega_0}\right), \quad (15)$$

where  $B_\infty = -i\sqrt{2\gamma_1}b^{\text{in}}/\gamma$ . Consequently Eq. (14) reads

$$\Theta(\tau) = \Theta_\infty(\tau) - \frac{\gamma}{g\omega_0} [\Theta_{\infty 0} - \Theta_\infty(\tau)]. \quad (16)$$

### 3. Null-stability zone

Consider the case of operating in the nullstability zone. Switching between SC and NC phases occurs when  $\Theta(t) = 1$ . At that time the mode amplitude  $B$  can be found from the value of  $\Theta_\infty$ . Using Eq. (16) one finds to first order in  $\gamma/g\omega_0$

$$\Theta_\infty = 1 + \frac{\gamma(\Theta_{\infty 0} - 1)}{g\omega_0}. \quad (17)$$

Using Eq. (7) and Eq. (10) one finds that the mode amplitude at switching, to first order in  $\gamma/g\omega_0$ , is given by

$$|B| = |B_0| \left\{ 1 + \frac{\gamma}{2g\omega_0} \left[ \left( \frac{B_\infty}{B_0} \right)^2 - 1 \right] \right\}. \quad (18)$$

where  $|B_0|^2 = \omega_0 g / 2\kappa\gamma_2\rho$  is the value of  $|B|^2$  for which  $\Theta_\infty = 1$ . We denote by  $B_s$  ( $B_n$ ) the value of  $|B|$  when a switching from the SC to the NC (NC to SC) phase occurs.

*a. SM Period* The SM period is denoted as  $\mathcal{T} = \mathcal{T}_s + \mathcal{T}_n$ , where  $\mathcal{T}_s$  ( $\mathcal{T}_n$ ) is the time, in which the system is in the SC (NC) phase. Using Eq. (15) one finds

$$\mathcal{T}_s = \frac{1}{\gamma_s} \log \frac{B_n - B_{\infty s}}{B_s - B_{\infty s}}; \quad \mathcal{T}_n = \frac{1}{\gamma_n} \log \frac{B_s - B_{\infty n}}{B_n - B_{\infty n}}. \quad (19)$$

Slightly above the first SM power threshold one has  $B_s \simeq B_{\infty s}$ . In this case one expects that  $\mathcal{T}_s \gg \mathcal{T}_n$ . Moreover writing  $\mathcal{T}_s$  as

$$\mathcal{T}_s = \frac{1}{\gamma_s} \left( \log \frac{B_{\infty s} - B_n}{B_{0s}} + \log \frac{B_{0s}}{B_{\infty s} - B_s} \right), \quad (20)$$

where  $B_{0s} = -i\sqrt{2\gamma_{1s}}b_0^{\text{in}}/\gamma_s$ ,  $b_0^{\text{in}}$  is the input amplitude associated with the first SM power threshold, and neglecting the first term, which is much smaller than the second one, and using Eq. (18) yield

$$\mathcal{T} \simeq \mathcal{T}_s \simeq -\frac{1}{\gamma_s} \log \left\{ \frac{B_{\infty s}}{B_{0s}} - 1 - \frac{\gamma}{2g\omega_0} \left[ \left( \frac{B_\infty}{B_0} \right)^2 - 1 \right] \right\}. \quad (21)$$

Thus, using the notation  $\vartheta = (b^{\text{in}} - b_0^{\text{in}})/b_0^{\text{in}}$  one finds that slightly above the first threshold, when  $\vartheta \ll 1$ , namely when regular SM with a relatively long period occurs, the SM period is given by

$$\mathcal{T} \simeq \frac{1}{\gamma_s} \log \frac{1}{\vartheta \left( 1 - \frac{\gamma}{g\omega_0} \right)} \simeq \frac{1}{\gamma_s} \log \frac{1}{\vartheta}. \quad (22)$$

Note that disregarding noise can not be justified very close to the first power threshold, since in that region the system is extremely sensitive to fluctuations.

*b. Spectral Density* The output signal reflected from the resonator is written as  $a^{\text{out}} = b^{\text{out}} e^{-i\omega_p t}$ , where  $b^{\text{out}}$  is a complex amplitude. According to the input-output relation, which relates the output signal to the input one<sup>26</sup>, the following holds

$$\frac{b^{\text{out}}}{\sqrt{\omega_0}} = \frac{b^{\text{in}}}{\sqrt{\omega_0}} - i\sqrt{\frac{2\gamma_1}{\omega_0}} B. \quad (23)$$

Above the first power threshold the amplitude  $B(t)$  is periodic,  $B(t) = B(t + \mathcal{T})$ . If the assumption  $\mathcal{T}_s \gg \mathcal{T}_n$  holds, one finds

$$B(t) \simeq B_n + (B_{\infty s} - B_n) (1 - e^{-\gamma_s t}), \quad (24)$$

where the time interval in which the hotspot is in NC phase is neglected. The power spectrum of the  $k^{\text{th}}$  harmonic of  $b^{\text{out}}$  is given by

$$P_k = \frac{1}{\mathcal{T}} \left| \int_0^{\mathcal{T}} b^{\text{out}}(t) e^{i\omega_k t} dt \right|^2, \quad (25)$$

TABLE I: Model's Parameters

	E15	E16		E15	E16
$\omega_0/2\pi$ [GHz]	5.7	3.8	$Q$ -factor	880	250
$d$ [nm]	200	8	$g$ [ $\times 10^{-3}$ ]	9.69	250
$P_{\text{pump}}$ [dBm]	-25.5	-49	$\rho$ [ $\times 10^{-9}$ ]	0.80	1180
$ S_{11} _{\text{th}}$ [dB]	-4.15	-13	$\gamma/g\omega_0$ [ $\times 10^{-3}$ ]	197	27

where  $\omega_k = 2k\pi/\mathcal{T}$ . Thus, using Eq. (23), the spectral density slightly above the first SM power threshold is given by

$$P(\omega_k) = \frac{2\gamma_1 (B_s - B_n)^2}{\mathcal{T}(\omega_k^2 + \gamma_s^2)}. \quad (26)$$

#### 4. Validity of the adiabatic approximation

We now return to the adiabatic approximation  $\gamma/g\omega_0 \ll 1$ , and examine its validity by estimating the value of the parameter  $g$  in Eq. (8). Consider the case where the nonlinearity originates by a hotspot of lateral area  $A_{\text{eff}}$ , forming in the microbridge. The heat capacity  $C$  of the hotspot can be expressed as  $C = C_v A_{\text{eff}} d$ , where  $C_v$  is the heat capacity per unit volume, and  $d$  is the thickness of the NbN film. By further assuming that the generated heat is cooled mainly down the substrate rather than along the film<sup>27</sup>, the heat transfer coefficient reads  $H = \alpha A_{\text{eff}}$ , where  $\alpha$  is the thermal surface conductance between the NbN film and the substrate. According to this notation Eq. (8) is expressed as  $g = \alpha/C_v d\omega_0$ . To obtain an estimate for the parameter  $\rho$  in Eq. (9), we evaluate the total dissipated power  $Q_t$  in the resonator at the first SM power threshold  $E_s$ , by assuming that the power dissipated in the microbridge is given by  $\kappa Q_t = \kappa(1 - |S_{11}|_{\text{th}})P_{\text{pump}}$ , where  $P_{\text{pump}}$  is the injected input power,  $|S_{11}|_{\text{th}}$  is the reflection coefficient at the first SM power threshold and  $\kappa \simeq 1$ . On the other hand, this equals to the heat flow from the microbridge to the substrate  $W = \alpha A_{\text{eff}} (T - T_0)$ . Thus Eq. (9) can be expressed as  $\rho = \alpha \hbar \omega_0 / C_v d \kappa Q_t$ . The value of  $\alpha$  and  $C_v$  parameters as estimated for NbN on a Sapphire substrate at temperature  $T = 4.2 \text{ K}$ <sup>27,28</sup>, are  $\alpha \simeq 12.5 \text{ W cm}^{-2} \text{ K}^{-1}$  and  $C_v \simeq 2.7 \times 10^{-3} \text{ J cm}^{-3} \text{ K}^{-1}$ . The various measured and calculated parameters are summarized in table I, which shows that the adiabatic assumption is justified for E16, and is marginal for E15. But as the above estimation does not take into account the direct contact between the sample and the liquid Helium, it is reasonable to assume that the adiabatic assumption is justified for E15 as well.

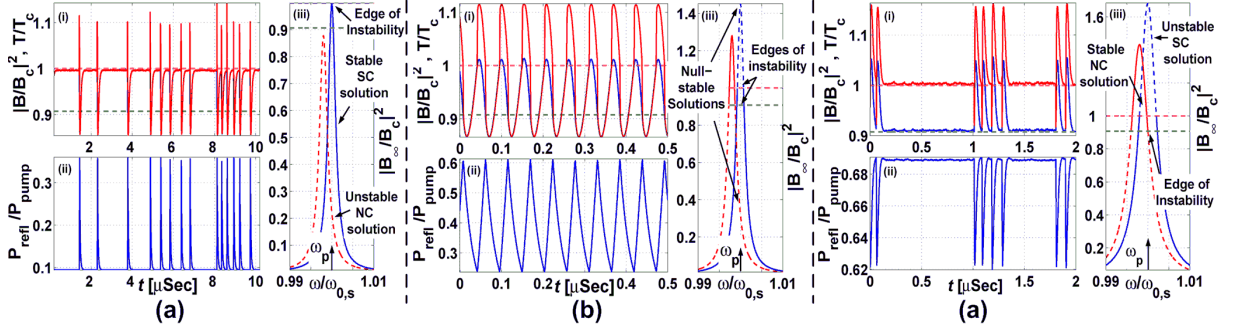


FIG. 7: (Color online) Numerical integration of the equations of motion of the model at three distinct pump powers (a) the first power threshold (b) some intermediate power between the first and second power thresholds, and (c) the second power threshold. Each panel has three subplots. Subplot (i) describes the normalized mode amplitude  $B_N$  (blue), and the normalized hotspot temperature  $T_N$  (red), as a function of time, where both are normalized by their critical values at which a transition from the SC to the NC phase occurs. Subplot (ii) plots the reflected power off the resonator  $P_{\text{ref}}$  normalized by the impinging pump power  $P_{\text{pump}}$ . Subplot (iii) describes the normalized steady state solution of the mode amplitude (Eq.(2)), as a function of the normalized frequency, for the case where it is decoupled from the bridge temperature. The solution is again normalized by its critical value  $E_s$ , and the frequency is normalized by the SC resonance frequency. The solid and dashed portions of the curves represent solutions which are stable and unstable respectively, according to the stability diagram in Fig. 5(b). The blue and red curves are solutions for the cases where the system is in the SC and the NC phase, respectively. The magenta and green dashed lines in subplots (i,iii) show  $E_s$  and  $E_n$  normalized by  $E_s$  respectively.

## V. NUMERICAL INTEGRATION

Following the discussion in section II, the numerical results presented for E15 are calculated by assuming a significant increase in the damping rate and a negligible shift in the resonance frequency as the critical temperature is exceeded, and the results presented for E16 are calculated by assuming the opposite case, where only  $\omega_0$  is temperature dependant.

Fig. 7 shows numerical integration results of the coupled Eq. (1) and Eq. (3), using the case where a shift in the resonance frequency occurs (E16). Results obtained by assuming a significant increase in the damping rate with no frequency shift are presented in Ref.<sup>15</sup>. The resonator is stimulated by an impinging pump tone at the SC resonance frequency. Panel (a) shows results that are calculated for a pump power in the first SM power threshold range. If the system would have been noiseless then both the mode amplitude and the temperature could reach a steady state. At this steady state the reflection from the resonator is relatively low as the pump frequency coincides with the resonance frequency. As this steady state is on the edge of instability, the thermal noise at a temperature of 4.2 K makes the system unstable and it occasionally falls off the edge and switches to the NC phase. When this happens, the dissipation slightly increases but more significantly, the resonance frequency shifts, and consequently the mode amplitude starts decreasing. As a result the heat production, which is proportional to the mode amplitude squared, decreases and thus when the excess heat is transferred to the substrate, and the temperature of the bridge decreases below the critical one, the resonator switches back to the SC state and a new buildup cycle of electromagnetic en-

ergy begins. Accordingly, the reflected power is low for most of the time, and these cycles are realized as sporadic but correlated spikes of the reflected power. The heat generated in such a spike, raises the probability for a sequential spike to occur, and thus induces a positive correlation between the spikes (bouncing). The dynamics of the relaxation cooldown of these spikes is similar, and thus their line-shapes also. The power range in which these spikes are triggered, and hence the width of the power threshold range, is governed by the noise intensity.

Panel (b) shows results calculated for some pump power in the range of the regular SM. The evolution of the system is similar to the one just described, with one major difference. When the system is in the SC phase the mode amplitude is built toward a nullstable state and thus a steady state is not achieved. As a result, regular oscillations occur without the assistance of noise, which in general, has a negligible impact in that power range.

Panel (c) shows results calculated for a pump power at the second SM power threshold while assuming a 15 K thermal noise and a slightly enhanced damping rate due to an average increase in the microbridge temperature. The behavior of the system at this threshold resembles the first one, but the SC and NC phases exchange roles. In this power range the resonator is in the NC, high reflective phase for most of the time and noise-induced spikes temporarily drive it to the SC, low reflective phase. The internal thermal noise at the second threshold is stronger than at the first one and consequently this power threshold range is wider.

Fig. 8 shows the envelope line-shape of the reflected power when a regular SM, having a frequency of approximately 6 MHz, occurs. The experimental data is seen



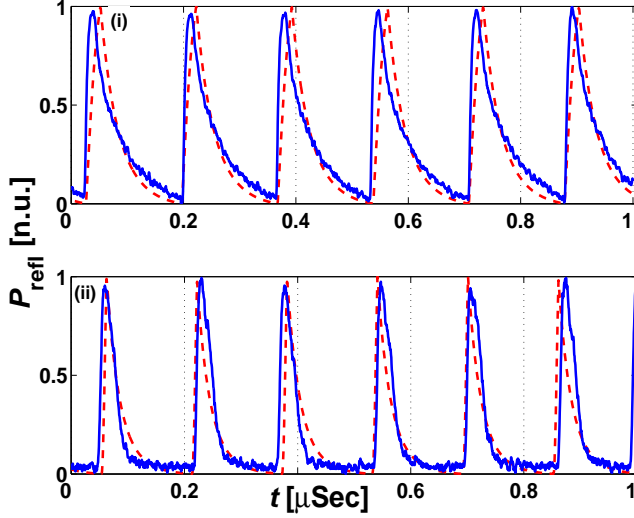


FIG. 8: (Color Online) SM reflected power line-shapes of experimental (blue) and the numerical integration of the model's equations of motion (dashed red) results, normalized by the maximum peak to peak value and the incident pump power respectively.

in blue, and the numerical integration results are seen in dashed red. The two subplots include data obtained with E15 (panel (i)) and E16 (panel (ii)), respectively. The numerical results were calculated using the corresponding parameters for each device as discussed above. The comparison shows a good match between the model and the experimental data for both cases.

## VI. ANALYTICAL RESULTS

Fig. 9 shows a comparison between the measured SM frequency and the one predicted by Eq. (22), for data taken with E15 (panel (i)) and E16 (panel (ii)) devices. Eq. (22) is expected to hold when the input power is slightly above the first SM power threshold. Indeed, when using an experimentally measured damping rate of  $\gamma_s = 26$  MHz for E16<sup>16</sup> and a fitted damping rate of  $\gamma_s = 23.1$  MHz for E15, the model yields a good agreement for both devices.

The spectral power density of the reflected power from the resonator is predicted by Eq. (26) for the case where the pump power is slightly above the first SM power threshold, namely regular SM with a rather low frequency occurs. This prediction is compared with typical experimental results, obtained with E15, in the upper subplot of Fig. 10. The noise has a negligible influence on the SM characteristics in that power range. On the other hand, the dynamics of the system is governed by the noise on the edge of the SM, as is demonstrated in Fig 7(a). The frequency domain of the numerical results at that region is compared with typical experimental results, ob-

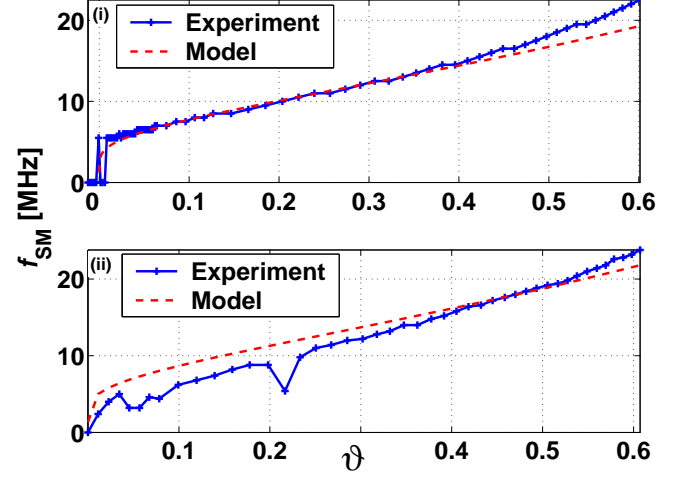


FIG. 9: (Color Online) SM frequency as a function of the normalized injected power  $\vartheta$ , measured with E15 (upper) and E16 (lower) devices.

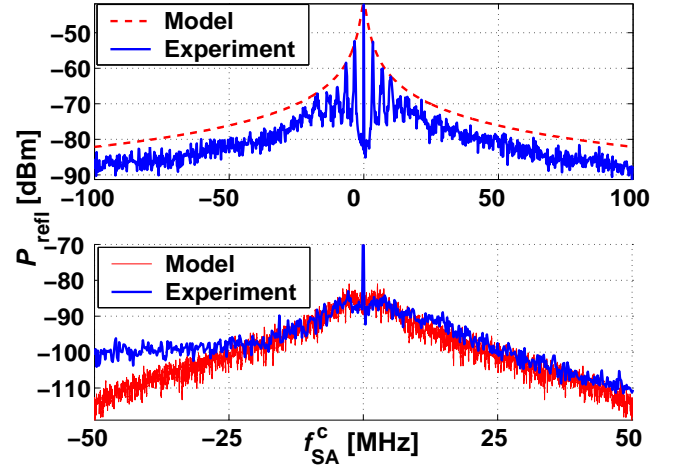


FIG. 10: (Color Online) The solid blue curves in the upper and lower subplots show typical SM experimental results in the frequency domain, obtained with E15 and E16 respectively. The dashed red curve presents the model prediction according to Eq. (26). The solid red line was obtained by numerically integrating the model's equations of motion at the first threshold power with nonvanishing noise (Fig 7(a)) and evaluating the spectral density.

tained with E16 in the lower subplot. Both comparisons show a good agreement. The numerical results indicate that the model predicts a strong noise rise near the SM power threshold. Theoretically, such noise amplification is expected to increase when the system is approaching a threshold of instability, where a linear theory predicts an unbounded increase of fluctuation<sup>29</sup>, which only saturates due to the high order nonlinear terms<sup>30</sup>. As predicted theoretically<sup>6</sup> the same mechanism generates large

signal amplification, as was indeed observed in Ref.<sup>14</sup>.

## VII. CONCLUSIONS

We report on a novel nonlinear behavior, where SM is generated in SC microwave stripline resonators. This phenomenon is robust and occurs with all of our devices, despite differences in geometry, and at various resonance frequencies in each device. A theoretical model according to which the SM originates by a thermal instability is proposed, to account for our findings. In spite of its simplicity the model exhibits a good quantitative agreement

with the experimental results. These devices can serve as ultra-low noise amplifiers with possible applications in the field of quantum data processing.

## Acknowledgments

We thank Ron Lifshitz, Mile Cross, Oded Gottlieb, and Steven Shaw for valuable discussions. This work was supported by the German Israel Foundation under grant 1-2038.1114.07, the Israel Science Foundation under grant 1380021, the Deborah Foundation, the Poznanski Foundation, and MAFAT.

- 
- \* Electronic address: segeve@tx.technion.ac.il
- <sup>1</sup> R. Movshovich, B. Yurke, P. G. Kaminsky, A. D. Smith, A. H. Silver, R. W. Simon, and M. V. Schneider, *Phys. Rev. Lett.* **65**, 1419 (1990).
  - <sup>2</sup> B. Yurke and E. Buks (2005), arXiv:quant-ph/0505018.
  - <sup>3</sup> E. Buks and B. Yurke, *Phys. Rev. A* **73**, 023815 (2005).
  - <sup>4</sup> E. Arbel-Segev, B. Abdo, O. Shtempluck, and E. Buks (2006), arXiv:quant-ph/0606099.
  - <sup>5</sup> I. Siddiqi, R. Vijay, F. Pierre, C.M. Wilson, M. Metcalfe, C. Rigetti, L. Frunzio, and M. H. Devoret, *Phys. Rev. Lett.* **93**, 207002 (2004).
  - <sup>6</sup> K. Wiesenfeld and B. McNamara, *Phys. Rev. A* **33**, 629 (1986).
  - <sup>7</sup> J. C. Lee, W. D. Oliver, T. P. Orlando, and K. K. Berggren, *IEEE Trans. Appl. Superconduct.* **15**, 841 (2005).
  - <sup>8</sup> D. W. Floet, E. Miedema, T. M. Klapwijk, and J. R. Gao, *App. Phys. Lett.* **74**, 433 (1999).
  - <sup>9</sup> G. N. Goltsman, A. Korneev, I. Rubtsova, I. Milostnaya, G. Chulkova, O. Minaeva, K. Smirnov, B. Voronov, W. Sysz, A. Pearlman, et al., *Phys. Status Solidi C* **2**, 1480 (2005).
  - <sup>10</sup> A. S. Clorfeine, *Appl. Phys. Lett.* **4**, 131 (1964).
  - <sup>11</sup> R. V. D'Aiello and S. J. Freedman, *Appl. Phys. Lett.* **9**, 323 (1966).
  - <sup>12</sup> S. A. Peskovatskii, I. I. Era, and O. I. Barilovich, *JETP Lett* **6**, 227 (1967).
  - <sup>13</sup> I. I. Eru, V. A. Kashchei, and S. A. Peskovatskii, *Sov. Phys. JETP* **31**, 416 (1970).
  - <sup>14</sup> E. Arbel-Segev, B. Abdo, O. Shtempluck, and E. Buks (2006), arXiv: cond-mat/0607262.
  - <sup>15</sup> E. Arbel-Segev, B. Abdo, O. Shtempluck, and E. Buks (2006), arXiv: cond-mat/0607259.
  - <sup>16</sup> E. Arbel-Segev, B. Abdo, O. Shtempluck, and E. Buks, *IEEE Trans. Appl. Superconduct.* **16**, 1943 (2006).
  - <sup>17</sup> K. Chang, S. Martin, F. Wang, and J. L. Klein, *IEEE Trans. Microwave Theory Tech.* **MTT-35**, 1733 (1987).
  - <sup>18</sup> D. Saeedkia, A. H. Majedi, S. Safavi-Naeini, and R. R. Mansour, *IEEE Microwave Wireless Compon. Lett.* **15**, 510 (2005).
  - <sup>19</sup> J. Zhang, W. Slysz, A. Verevkin, O. Okunev, G. Chulkova, A. Korneev, A. Lipatov, G. N. Goltsman, and R. Sobolewski, *IEEE Trans. Appl. Superconduct.* **13**, 180 (2003).
  - <sup>20</sup> A. V. Gurevich and R. G. Mints, *Rev. Mod. Phys.* **59**, 941 (1987).
  - <sup>21</sup> A. M. Kadin and M. W. Johnson, *Appl. Phys. Lett.* **69**, 3938 (1996).
  - <sup>22</sup> J. Kitaygorsky, J. Zhang, A. Verevkin, A. Sergeev, A. Korneev, V. Matvienko, P. Kouminov, K. Smirnov, B. Voronov, G. Goltsman, et al., *IEEE Trans. Appl. Superconduct.* **15**, 545 (2005).
  - <sup>23</sup> P. Suret, D. Derozier, M. Lefranc, J. Zemmouri, and S. Bielański, *Phys. Rev. A* **61**, 021805 (2000).
  - <sup>24</sup> B. Abdo, E. Segev, O. Shtempluck, and E. Buks, *Phys. Rev. B* **73**, 134513 (2006).
  - <sup>25</sup> B. Abdo, E. Segev, O. Shtempluck, and E. Buks (2005), arXiv:cond-mat/0501114 v2.
  - <sup>26</sup> C. W. Gardiner and M. J. Collett, *Phys. Rev. A* **31**, 3761 (1985).
  - <sup>27</sup> M. W. Johnson, A. M. Herr, and A. M. Kadin, *J. Appl. Phys.* **79**, 7069 (1996).
  - <sup>28</sup> K. Weiser, U. Strom, S. A. Wolf, and D. U. Gubser, *J. Appl. Phys.* **52**, 4888 (1981).
  - <sup>29</sup> K. Wiesenfeld, *J. Stat. Phys.* **38**, 1071 (1985).
  - <sup>30</sup> Y. Kravtsov and E. Surovyatkina, *Phys. Lett. A* **319**, 348 (2003).